2023 IEEE International Conference on Robotics and Automation (ICRA 2023)
May 29 - June 2, 2023. London, UK

Modeling of a Robotic Transcatheter Delivery System

Namrata U. Nayar*, Ronghuai Qi, and Jaydev P. Desai, *Fellow IEEE*

Abstract— **Intracardiac transcatheter systems guided by advanced imaging modalities are gaining popularity in treating mitral regurgitation in non-surgical candidates. Robotically steerable transcatheter systems must use model-based control strategies to ensure safer and more effective transcatheter procedures with less trauma while using smaller control gains. In this paper, a 4-DoF robotically steerable tendon-driven robot was fabricated, and the relationship between the tendon displacement and the joint angle was derived. This relation was derived in two parts to make this approach applicable to any other catheter system. A model was derived to determine the tendon tensions needed to achieve desired joint angles. Then, the tendon characteristics were studied, and a tendon elongation (TE) model was derived as a function of tendon length. Executing the modeling process in two steps makes it easy to introduce additional parameters like length, friction, and pose, to characterize complex systems like catheters. The TE model was used to actuate the joints of the robot and RMSE was computed to characterize its performance. Also, PID control was used along with the TE model to improve the system's performance, and the contribution of the model and the controller in the system was recorded.**

I. Introduction

Mitral regurgitation (MR) is a type of heart disease in which the valve between the left atrium (LA) and left ventricle (LV) does not close properly during systole, causing the backflow of blood from the LV to LA. 1.7 % of US adult population and 9.3 % of adults over the age of 75 suffer from MR [1], [2]. The mortality rate of patients can increase to 57 % if left untreated [3]. Half of the MR patients are not recommended an open-heart surgery (OHS) due to their age and possibilities of post-operative complications [4]. Minimally invasive mitral valve surgery (MIMVS) has been proven to be a feasible alternative to OHS due to low perioperative morbidity and short-term mortality [5]–[7]. Consequently, MIMVS has become popular worldwide because of its excellent short-term and long-term results [7]–[9].

To treat MR, transcatheter mitral valve repair is preferred over transcatheter mitral valve replacement to avoid LV outflow tract obstruction [10]. Currently, two commercial catheter systems, including MitraClip™ device (Abbott Laboratories, IL) and Edwards Pascal transcatheter valve repair system (Edwards Lifesciences, CA), can be used for transcatheter edge-to-edge repair [11]. However, these commercially available catheter systems are manually operated and have one catheter for steering (bending) and another catheter, put through the first, for remote torquing, causing overexposure of clinical staff to radiation [12]–[14] and less torque transmission efficiency [15].

In our prior work [16], [17], we have developed prototypes of the robotic transcatheter delivery system for mitral valve implant to address the problems above. We focused on hardware design and kinematics without considering tendon elongation modeling in these works. However, in tendon-driven robotically steerable catheters with constraints on tendon sizing, tendon elongation cannot be assumed to be negligible, as done for larger tendons [18]. Existing research mainly focuses on using metal tendons made of Nitinol [19], stainless steel [20], and Tungsten [21], and tendon elongation models [19], [20], [22] are suitable for these materials. However, metal wires or ropes have higher stiffness, resulting in low curvature and tendon force transmission failure in meso-scale robots with tortuous tendon routing paths. Non-metallic tendon materials, such as Kevlar, Nylon, Polyester, and Polypropylene [23], can be used for force transmission and overcome the above-mentioned problems. However, limited research has investigated non-metallic tendon elongation models, in small-scale robots. Bai et al., [24] evaluated the performances of existing cyclic models on large-rupture strain fiber-reinforced polymer (LRS FRP)-confined concrete and developed a new cyclic stress-strain model by defining two critical parameters (plastic strain and stress degradation). However, this paper was focused on developing a model to analyze the cyclic loading of concrete structures.

In this paper, a 4-DoF robotically steerable tendon-driven robot was fabricated, and the relationship between the tendon displacement and the joint angle was modeled while accounting for the tendon elongation. This model was derived in two steps: first, the relationship between tendon tension and joint angle was determined for various joints; second, the tendon characteristics were studied to derive a TE model as a function of tendon length. The advantages of characterizing tendon elongation include: 1) possible elimination of additional feedback sensors (tendon tension sensors), 2) determining the correct amount of tension to apply for preconditioning the tendon before the procedure, and 3) optimizing the actuation system design, to ensure simplicity and compactness. Executing the modeling process in two steps also makes it straightforward to introduce additional parameters like length, friction, and pose to characterize complex systems like catheters. Finally, the derived TE (tendon elongation) model was used as a feedforward input

This work was supported in part by the National Heart, Lung, And Blood Institute of the National Institutes of Health under Award Number R01HL140325. The content is solely the responsibility of the authors and does not necessarily represent the official views of the National Institutes of Health.

The authors are with the Medical Robotics and Automation (RoboMed) Laboratory, Wallace H. Coulter Department of Biomedical Engineering, Georgia Institute of Technology, Atlanta, GA, USA.

*Namrata U. Nayar is the corresponding author (nnayar7@gatech.edu).

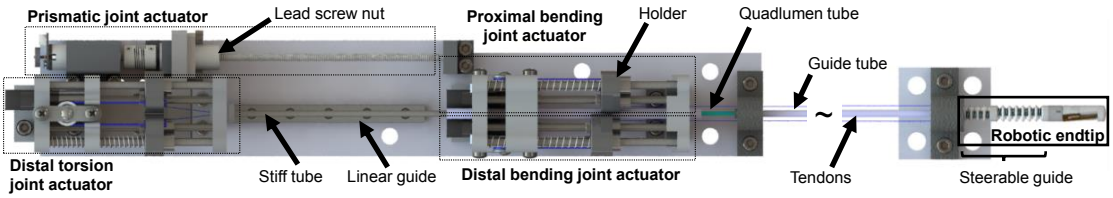

Fig. 1: Schematic of the robotic system.

to actuate the robot, with and without a PID controller, and the contribution of the model and controller was recorded.

The paper is organized as follows: Section II introduces the design of the robotic system, Section III discusses the tendon elongation model, joint actuation force model, and kinematic modeling of the robot joints, and Section IV contains experiments and results. Finally, the conclusions and future work are summarized in Section V.

II. Design

The robotic transcatheter delivery system has an endtip that is manipulated using an actuation system as shown in Fig. 1. The robot at the distal end has an outer diameter of 5.7 mm, which makes it feasible to introduce it into the left atrium through a 24Fr steerable outer sheath. The robot (see Fig. 2) consists of 4 joints: proximal bending joint, distal bending joint, prismatic joint, and distal torsion joint. Given below is a brief description of the joint functionalities and characteristics.

A. Joint Actuation and Function

1) Proximal Bending Joint: This joint is actuated to sweep the implant along the MV annulus plane in the anterior-posterior direction. It can align the implant to the MR jet. This motion is necessary to deploy the implant at the right location on the MV for maximum reductions in MR. However, this bending joint is actuated after the distal bending joint and comprises of three concentric 3D printed segments (n=3) with a total steerable length of 8.52 mm. This joint can achieve bidirectional bending of 90°.

2) Distal Bending Joint: The distal bending joint is actuated first in the transcatheter delivery procedure. This joint helps reach the MV opening from the transseptal puncture location by facilitating a sharp turn within the left atrium. The bending of this joint and introduction of the robotic catheter into the left atrium is performed simultaneously to reduce trauma to internal cardiac tissue. The joint aligns the implant perpendicular to the MV plane and comprises of six segments, with a total steerable length of 15.66 mm. It can achieve bidirectional bending of 120°.

3) Prismatic Joint: Actuation of the prismatic joint advances the implant under the MV entirely for proper deployment. This joint can be advanced up to 60 mm.

4) Distal torsion Joint: After the implant is advanced under the MV, the distal torsion joint is used to orient the implant to the MV leaflet for effective grasping. Motion capability of ±45° is needed to fine-tune the orientation of the implant to the MV leaflets but this joint can achieve up to

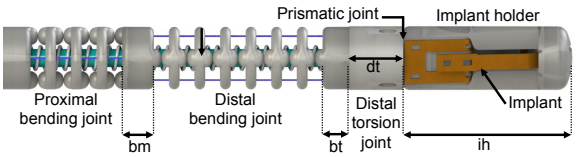

Fig. 2: Schematic of the robot endtip

±75°. Once the implant is appropriately positioned, oriented, and significantly reduces MR, it is deployed onto the MV.

B. Actuation System

The actuation system (see Fig. 1) consists of stationary (proximal and distal bending joint actuators) and moving components (prismatic and distal torsion joint actuators). The stationary components control the steerable guide that positions the implant over the MV opening, whereas the moving components control the advancement and orientation of the implant for proper grasping.

1) Stationary components: The proximal and distal bending joint actuators (PBJA and DBJA) control the robot's steerable guide. The steerable guide comprises of the proximal and distal bending joint, as shown in Fig. 1. The proximal and distal bending joints have bending planes perpendicular to each other. Each bending joint is actuated using two antagonistic tendons. Both pairs of antagonistic tendons, routed from the robot to the actuation system, are attached to their respective actuator, as shown in Fig. 1. Each actuator has two holders attached to the two antagonistic tendons of the joint. The holders, connected by a pulley system, move in opposite directions by the same amount, hence pulling one and releasing the other antagonistic tendon simultaneously. One of the holders is actuated by a DC motor (Maxon Precision Motor, gear ratio 64:1, MA), while the connection between the holders is held in tension using a compression spring.

2) Moving components: The moving components of the actuation system comprise of the prismatic joint actuator (PJA) and distal torsion joint actuator (DTJA), as shown in Fig. 1. The lead screw nut of the PJA is attached to the DTJA. When the prismatic joint is actuated by a DC gearmotor (Pololu motor, gear ratio 100:1, NV), the DTJA, mounted on a linear guide, is translated simultaneously. The stiff tube attached to the DTJA contains the quadlumen tube that is advanced to actuate the prismatic joint of the robot. The quadlumen tube also routes the antagonistic distal torsion tendons to the DTJA. The torsion joint is actuated similarly to the bending joints as described above.

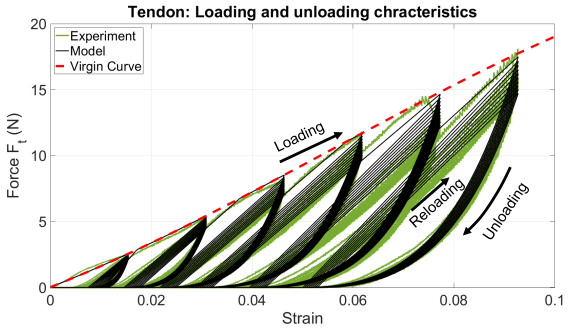

Fig. 3: Cyclic loading to characterize the UHMWPE actuation tendon

III. Modeling

A. Tendon Elongation

In this paper, we choose PE braided line (Hercules, CA) as the tendon because it is made from ultra-high-molecular-weight polyethylene (UHMWPE), which has low friction, high strength, great abrasion resistance, small diameter, and high flexibility. The tendon we use does undergo elongation due to tendon tension. The relationship between tendon tension and elongation is non-linear and difficult to characterize. Therefore, to understand the tendon elongation characteristics, we gathered tendon tension and elongation data for cyclic loading of the tendon. During the tendon elongation characterization experiment, initially the tendon tension is zero and the tendon is kept in a straight configuration. The experiment involves gradually elongating 65 mm of the tendon at a rate of 0.05 mm/sec. We subjected the tendon to 10 cycles each, of tendon elongations equal to n mm, where n=1, 2, ..., 6, as shown in Fig. 3. The red dotted line in the figure denotes the envelope curve of the material. If the material is continuously loaded without unloading, it follows the envelope curve. If it is unloaded and reloaded again, it follows a different path until the reloading curve intersects with the envelope curve, at which point it follows the envelope curve again.

The green line in Fig. 3 shows the experimentally gathered data depicting the relationship between tendon tension and elongation within the operating range of tendon tension we use. The black line depicts the model we used to characterize the tendon elongation described below.

During cyclic loading, the tendon goes through 3 major phases: loading, unloading, and reloading.

1) Loading: During loading, the tendon characteristics follow the envelope curve. The tendon is never in the loading phase for forces lower than the maximum force it has been subjected to. The loading curve for the tendon we used can be represented by a 3rd-degree polynomial. Also, ε_{env} and F_{env} denote tendon strain and tension, respectively, when the tendon is in the loading phase (envelope curve).

2) Unloading: During unloading, the tendon does not return to zero strain for zero tension as it is permanently deformed by some amount. The amount of permanent deformation the tendon has undergone is given by ε_{pl}. During unloading, the tendon characteristics follow a path given by:

$$F = a\varepsilon^q + b\varepsilon + c \tag{1}$$

where, q is defined as $a_n\varepsilon_{ul}+b_n$. Equation (1), a polynomial function of order q, was chosen to represent the unloading curve as: 1) the slope of an individual unloading curve increases with strain and 2) the rate of change of slope is higher for larger strain values (ε_{ul}). Other flexible tendons displaying comparable cyclic loading characteristics could be modeled similarly. Here, ε_{ul} represents the strain value when the tendon starts unloading, and F_{ul} is the corresponding tension in the tendon at this point. Also, the ratio ε_{pl} to ε_{ul} is given by γ, where γ lies between 0 and 1. Assuming that the slope at $(\varepsilon_{pl}, 0)$ is zero and the curve passes through $(\varepsilon_{ul}, F_{ul})$, a, b, and c can be given by:

$$a = \frac{F_{ul}}{\varepsilon_{ul}^q - \varepsilon_{pl}^q - q(\varepsilon_{pl}^{q-1})(\varepsilon_{ul} - \varepsilon_{pl})} \tag{2}$$

$$b = -q(\varepsilon_{pl}^{q-1})a \tag{3}$$

$$c = -a\varepsilon_{pl}^q - b\varepsilon_{pl} \tag{4}$$

3) Reloading: This phase always follows unloading. The curve followed by the tendon during reloading is very linear and is characterized by a line of slope *m*, connecting the points, $(\varepsilon_{pl} + (n_c - 1)\beta, 0)$, and $(\varepsilon_{ul}, \phi^{n_c-1}F_{ul})$. ϕ is a number between 0 and 1. If the tendon is unloaded again before reaching the envelope curve, it shifts slightly to the right with every reloading cycle. This shift can be seen in the 10 cycles shown in Fig. 3. Hence, we develop a model to characterize tendon elongation using Algorithm 1. The optimized constant parameters obtained from this algorithm, ϕ=0.9810, γ=0.4605, a_n=7.7751, b_n=5.4876, β=0.00035, p_1=-2000 N, p_2=6000 N, p_3=150 N, p_4=0.03 N, are used to get the model output shown in Fig. 3. These parameters are found using the *fminsearch()* function in MATLAB.

4) Tendon Elongation Model: For the TE model, we assume that ϕ=1 and β=0 from the second reloading cycle. Assuming these values makes the unloading and reloading curves retrace the same path, simplifying the model. So for a given tendon tension value, we can extract the tendon strain, using lines 6, 14, or 23 from Algorithm 1, by keeping track of the phase the tendon is in. The tendon elongation can be calculated once the strain and tendon length are known.

B. Joint Actuation Force

To use the TE model derived above, it is crucial to know the tendon tension needed to actuate the joints. Deriving a relationship between tendon tension and joint bending angle will help us establish a relationship between our joint space (bending joint angles) and actuator space (tendon displacement). To model these relationships, we experimentally gathered the bending joint angle and the tendon tension needed to actuate it. The experimental setup and input used to gather the data are given in Fig. 4(a).

In Fig. 4(b-i) and (b-ii), the green line denotes the experimental data. It can be observed that the loading curve profile does not change and remains consistent for the whole range of bending angles. This curve can be easily represented using a 3rd degree polynomial. However, the

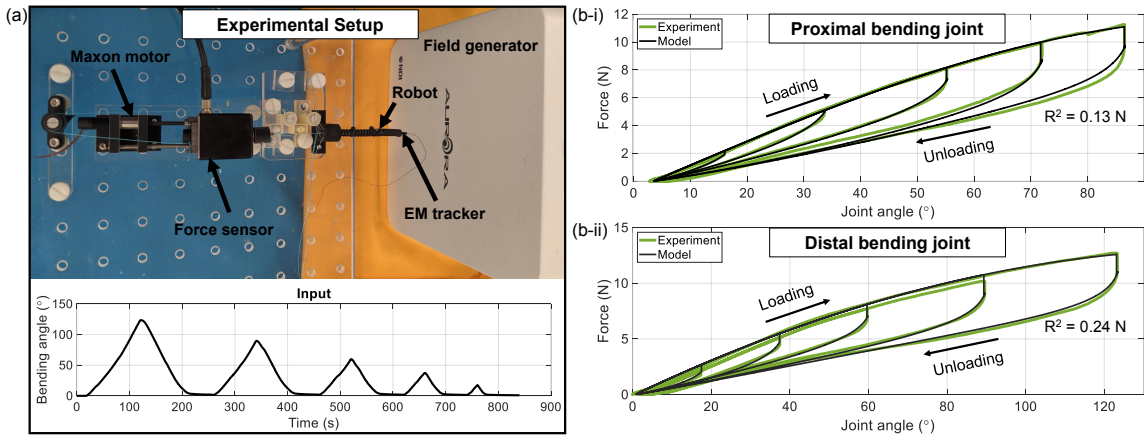

Fig. 4: (a) The experimental setup and (b) joint actuation tendon tension data gathered for given bending angles: (b-i) proximal bending joint and (b-ii) distal bending joint.

Algorithm 1 Model to predict tendon elongation

$n_c \leftarrow 0, \quad r \leftarrow 0, \quad flag \leftarrow 0, \quad \varepsilon_{env} = 0, \quad F_{env} = 0$
for $sample = 1, 2, \ldots$ **do**
  if $n_c = 0$ **then** ▷ Loading
    if $flag = 1$ **then** ▷ Started?
      $flag = 0$
    $F = p_1\varepsilon^3 + p_2\varepsilon^2 + p_3\varepsilon + p_4$
    if $\dot{\varepsilon} \leq 0$ **then** ▷ Unloading?
      $flag = 1$
      $n_c = n_c + 1, \quad \varepsilon_{env} = \varepsilon, \quad F_{env} = F$
  else if $n_c > 0$ && $r = 0$ **then** ▷ Unloading
    if $flag = 1$ **then** ▷ Started?
      $flag = 0$
      Update parameters a, b, c, q and ε_{pl}
    $F = a\varepsilon^q + b\varepsilon + c$
    if $\varepsilon < \varepsilon_{pl}$ **then** ▷ Minimum strain
      $\varepsilon = \varepsilon_{old}, \quad F = F_{old}$
    else if $\dot{\varepsilon} > 0$ **then** ▷ Reloading?
      $r = 1, \quad flag = 1, \quad \varepsilon_{re} = \varepsilon, \quad F_{re} = F$
  else if $n_c > 0$ && $r = 1$ **then** ▷ Reloading
    if $flag = 1$ **then** ▷ Started?
      $flag = 0$
      Update parameters m
    $F = F_{re} + m(\varepsilon - \varepsilon_{re})$
    if $\dot{\varepsilon} < 0$ **then** ▷ Unloading?
      $r = 0, \quad n_c = n_c + 1, \quad flag = 1$
    if $F > p_1\varepsilon^3 + p_2\varepsilon^2 + p_3\varepsilon + p_4$ **then** ▷ Loading?
      $n_c = 0, \quad r = 0, \quad flag = 1$
  if $F > F_{env}$ **then** ▷ Update max F
    $F_{env} = F$
  if $\varepsilon > \varepsilon_{env}$ **then** ▷ Update max strain
    $\varepsilon_{env} = \varepsilon$
  Optimize $\phi, \gamma, a_n, b_n, \beta, p_1, p_2, p_3, p_4$
  $F_{old} \leftarrow F$
  $\varepsilon_{old} \leftarrow \varepsilon$

unloading curve differs slightly and depends on the final bending angle to which the joint was actuated. It can be seen that the profile of the unloading curve looks like a scaled segment of the $tanh^{-1}()$ function. With this observation, using the Algorithm 2, we propose a model to characterize the relationship between tendon force and bending joint angle for both the proximal and distal bending joint. The algorithm is as follows:

Algorithm 2 F_t as a function of θ_b

if $\dot{\theta_b} \geq 0$ **then** ▷ Loading
  $F_t \leftarrow p_3\theta_b^3 + p_2\theta_b^2 + p_1\theta_b + p_0$
else ▷ Unloading

$$c_1, c_2 = \begin{cases} p_6, p_7 & \text{if } \theta_b \leq p_4 \\ p_8, p_9 & \text{if } \theta_b \leq p_5 \\ p_{10}, p_{11} & \text{otherwise} \end{cases}$$

$$S \leftarrow \max\left(0, \frac{p_3\theta_b^3 + p_2\theta_b^2 + p_1\theta_b + p_0}{c_1}\right)$$

$$F_t \leftarrow S\, tan^{-1}\left(\left(\frac{\theta_b}{(b_{ul}+0.01}\right)^{c_2}\right)$$

Optimize p_0, p_1, p_2, p_3 using the loading curve
Optimize $p_4, p_5, p_6, p_7, p_8, p_9, p_{10}, p_{11}$ using whole data

Using this algorithm the loading curve parameter values were computed to be: $(p_0, ..., p_3)$ = (-0.61, 0.18, -1.29e-05, -5.25e-06) for the proximal bending joint and $(p_0, ..., p_3)$ = (-0.09, 0.17, -5.02e-04, -2.12e-07) for the distal bending joint. For the unloading curve the parameter values were computed to be $(p_4, ..., p_{11})$ = (40.06, 61.03, 4.08, 0.02, 5.26, 0.01, 4.70, 0.03) for the proximal bending joint and $(p_4, ..., p_{11})$ = (40, 64.50, 4, 0.05, 5.26, 0.01, 5.54, 0.01) for the distal bending joint. The model output is plotted in Fig. 4(b-i)-(b-ii), and the RMSE is found to be 0.13 N for the proximal bending joint and 0.24 N for the distal bending joint.

C. Kinematics of the Robot

The base frame and task frame of the robot are shown in Fig. 5, as $\{F_{rb}\}$ and $\{F_{rt}\}$. The pose and orientation of the task frame of the robot with respect to the base frame can be derived using the product of exponentials. The derived pose

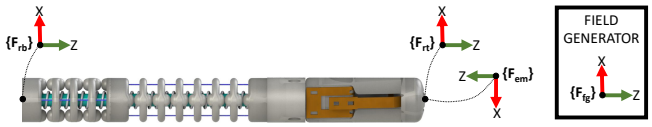

Fig. 5: Reference frames of the robot and EM tracking system

and orientation is given by:

$$g_{st} = \begin{bmatrix} R_{3\times3} & p_{3\times1} \\ 0 & 1 \end{bmatrix} \tag{5}$$

where, R and p are given by:

$$R = \begin{bmatrix} c_t c_{db} & -s_t c_{db} & s_{db} \\ s_t c_{pb} + s_{db} s_{pb} c_t & c_t c_{pb} - s_{db} s_{pb} s_t & -s_{pb} c_{db} \\ s_t s_{pb} - s_{db} c_{pb} c_t & c_t s_{pb} - s_{db} c_{pb} s_t & c_{pb} c_{db} \end{bmatrix} \tag{6}$$

$$p = \begin{bmatrix} s_{db}(e_l + \delta) + \frac{b_2}{\theta_{db}}(1 - c_{db}) \\ s_{pb}(bm + c_{db}(e_l + \delta)) + b_2 \frac{s_{db} s_{pb}}{\theta_{db}} - b_1 \frac{1+c_{pb}}{\theta_{pb}} \\ c_{pb}(bm + c_{db}(e_l + \delta)) + b_2 \frac{s_{db} c_{pb}}{\theta_{db}} + b_1 \frac{s_{pb}}{\theta_{pb}} \end{bmatrix} \tag{7}$$

Here, $c_x = \cos(\theta_x)$ and $s_x = \sin(\theta_x)$. Also, the joint parameters ih, dt, bt, b_2, bm, and b_1 are equal to 15 mm, 5 mm, 2 mm, 15.66 mm, 2 mm, and 8.52 mm, respectively. The rigid end length, $e_l = ih + dt + bt$. The joint angles, θ_{pb}, θ_{db}, and θ_t, and the prismatic motion, δ, can be computed using the orientation matrix, R, and the position vector, p. Here, θ_{pb}, θ_{db}, and θ_t, denote the proximal bending, distal bending, and distal torsion joint angle. They are calculated as given below:

$$\theta_{db} = \arcsin(R_{(1,3)}) \tag{8}$$

$$\theta_{pb} = \arctan\left(\frac{-R_{(2,3)}}{c_{db}}, \frac{R_{(3,3)}}{c_{db}}\right) \tag{9}$$

$$\theta_t = \arctan\left(\frac{-R_{(1,2)}}{c_{db}}, \frac{R_{(1,1)}}{c_{db}}\right) \tag{10}$$

$$\delta = \frac{1}{s_{db}}\left(p_{(1,1)} - \frac{b_2(1 - c_{db}))}{\theta_{db}}\right) - e_l \tag{11}$$

The pure kinematics (PK) equation relating the tendon displacement to joint bending angle, θ_b, is given by:

$$TD_b = 2(n+1)\left(t(1 - \cos\frac{\theta_b}{2(n+1)}) + a_b \sin\frac{\theta_b}{2(n+1)}\right) \tag{12}$$

where, n = 3 or 6, t = 0.69 mm , and a_b = 2.1 mm, are the number of bending segments in the joint, half the gap in between two segments, and the radial distance from the center to the point where the tendons are routed (the moment arm), respectively. The pure kinematics equation (PK model) relating the tendon displacement to the torsion joint angle, θ_t, is given by:

$$TD_t = r\theta_t \tag{13}$$

where, r = 2.1 mm is the radius of the tube around which the distal torsion tendons are routed.

IV. Experiments

A. Joint Space Control

In this experiment, we aim to control the two bending joints of the robot using EM tracker feedback while using the TE model and PK model. The PK model just uses equation (12) and neglects tendon elongation, whereas the TE model sums up TD_b (equation (12)) and the tendon elongation as computed in section III-A.4. The length of the tendon used to actuate these joints is 350 mm, which is a parameter needed to get the TE model results. The results for this experiment are shown in Fig. 6.

First, we actuate the proximal bending joint using the TE model and PK model to record its response and compare it to the desired bending angle, see Fig. 6(a-i). The RMSE for these experiments were found to be 4.8° and 21° degrees. Hence, adding the tendon elongation component has helped improve the proximal bending joint model. Moreover, to improve the performance, PID control (P:0.01, I:0.2, D:0.0001) is used along with the models (TE and PK), as shown in Fig. 6(a-ii). The RMSEs for these experiments were significantly lower and were found to be 0.88° and 2.53° degrees for the TE and PK models, respectively.

Upon reviewing the contribution of the controller to the experiment using the model and PID control (see Fig. 6(a-iii)), we noticed that we require a significantly lower controller inputs while using the TE model was instead of the PK model. Therefore, the robotic joints can be controlled accurately using smaller controller gains while using the TE model unlike the PK model (deviations appear in the return path). Also, modeling the system and using lower controller gains makes the system more reliable and better for surgical procedures. The same set of experiments were performed for

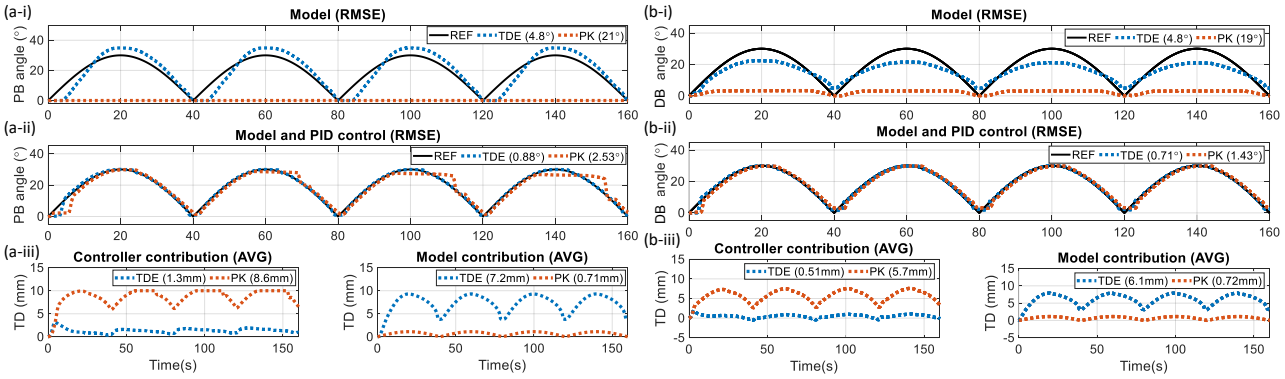

Fig. 6: Results from the joint space control experiment. Proximal bending joint (a-i) actuated using the model, and (a-ii) controlled using the model and a PID controller. The model and controller contributions are given in (a-iii) and (a-iv). Similar distal bending joint experiments were performed (b-i)-(b-iv).

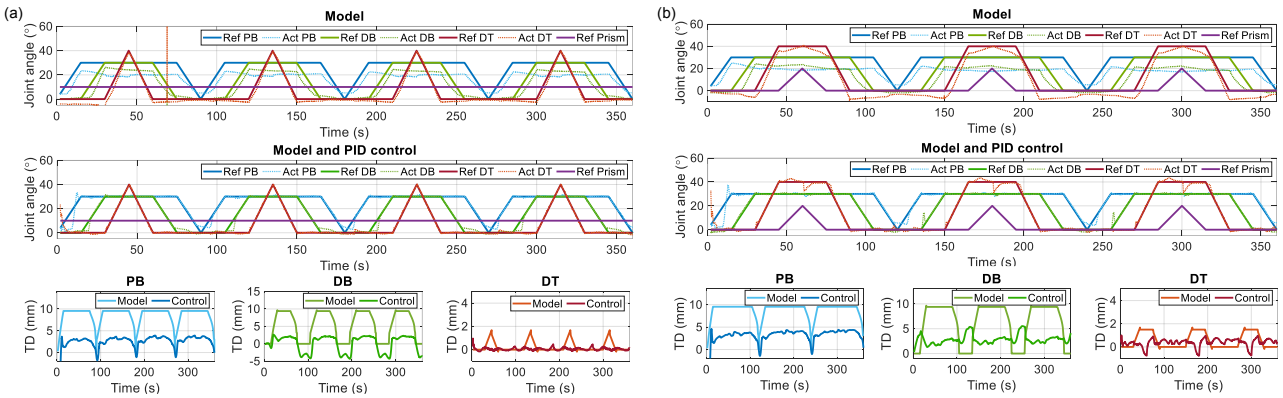

Fig. 7: Entire robot motion validation: with prismatic joint angle being (a) constant at 20 mm, and (b) variable.

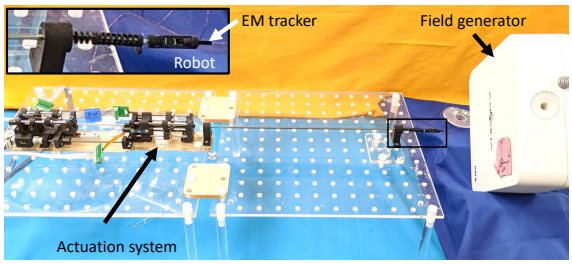

Fig. 8: Experimental setup for joint space control of the robot.

the distal torsion joint, and the results indicate similar trends (see Fig. 6(b-i)-(b-iii)).

TABLE I: RMSE values of joint angles.

	θ_{pb} (degrees)		θ_{db} (degrees)		θ_t (degrees)	
δ (mm)	M	M+Ctl	M	M+Ctl	M	M+Ctl
0	8.08	2.5	8.23	1.3	2.46	1.04
10	8.28	2.10	5.88	1.22	2.03	1.27
20	8.71	2.03	5.33	1.67	2.44	1.16
Variable	10.08	2.1	8.1	1.03	5.52	1.91

Note: M stands for model, and Ctl stands for Control

B. Entire Robot Motion Validation

In this experiment, we attempted to control the tendon-driven joints using the TE model, with and without PID control. We obtain the end effector's pose and orientation feedback from the EM tracker and transform it into the robot's base frame. As derived in equations (10)-(13), we extract the joint angles from the orientation matrix, R, and use these values as actual joint angle feedback. The experimental setup for this experiment is shown in Fig. 8. The TE model is used to compute the necessary tendon displacement values for the desired bending joint angles. The tendon displacement for the torsion joint is computed using the PK model and deadband compensation as the tendon tension required to actuate is small in the given configuration and results in negligible tendon elongation. For the experiment, the robot is actuated using the TE model and then actuated with the same reference inputs, using the TE model and PID control. The results for these experiments are given in Table I and Table II. The same two experiments are repeated for constant prismatic joint values equal to 0 mm, 10 mm, and 20 mm (see Fig. 7(a)), and variable prismatic joint values (see Fig. 7(b)). Finally, for the experiment where the TE model and PID control is used together, the contribution of the model and the PID controller was recorded and these values can be found in Table II. The experimental setup for these experiments is shown in Fig. 8.

TABLE II: Contribution of model and controller to actuate the joints.

	θ_{pb} (degrees)		θ_{db} (degrees)		θ_t (degrees)	
δ (mm)	M	Ctl	M	Ctl	M	Ctl
0	0.74	0.26	0.75	0.25	0.6	0.4
10	0.74	0.26	0.74	0.26	0.69	0.31
20	0.75	0.25	0.71	0.29	0.73	0.27
Variable	0.72	0.28	0.69	0.31	0.55	0.45

V. Conclusions

In this paper, we proposed and fabricated a 4-DoF robotically steerable tendon-driven robot and derived a relationship between the tendon displacement and the joint angle. This relationship was derived in two parts. First, a model was derived to determine the tendon tensions needed to achieve the desired joint angles. Second, the tendon characteristics were studied, and a TE model was derived as a function of tendon length. The TE model was used as a feedforward input and RMSE values were collected for both the bending joints when actuated with and without PID control.

Moreover, the entire robot validation is performed using feedback from an EM tracker to control the tendon-driven joints of the robot simultaneously. It was observed that when the TE model and PID controller were used to control the entire robot, the TE model contributed to $\sim$70% of the total effort. Therefore, while using the TE model smaller control gains would be enough to control the robot joints improving the stability of the robotic system. Higher errors were observed during the entire robot validation, and this could be due to coupling effects, ignoring the shift parameter β, not aligning the robot base frame to the field generator frame accurately, or hysteresis. In our future work, we will evaluate: 1) the effects of catheter configuration, hysteresis, and tendon sheath friction, which would be accounted in the joint actuation force model, 2) the tendon behavior at 37°C and in an operating environment where blood can coagulate, and 3) the effect of external perturbations, lubrication changes, and pulsatile flow. Finally, ultrasound feedback will be used instead of EM tracking feedback for closed-loop control.

REFERENCES

[1] V. T. Nkomo, J. M. Gardin, T. N. Skelton *et al.*, "Burden of valvular heart diseases: A population-based study," *The Lancet*, vol. 368, no. 9540, pp. 1005–1011, 2006.

[2] D. Mozaffarian, E. J. Benjamin, A. S. Go *et al.*, "Executive summary: Heart disease and stroke statistics–2016 update: A report from the american heart association," *Circulation*, vol. 133, no. 4, pp. 447–454, 2016.

[3] G. Cioffi, L. Tarantini, S. De Feo *et al.*, "Functional mitral regurgitation predicts 1-year mortality in elderly patients with systolic chronic heart failure," *Eur. J. Heart Fail.*, vol. 7, no. 7, pp. 1112–1117, 2005.

[4] M. Mirabel, B. Iung, G. Baron *et al.*, "What are the characteristics of patients with severe, symptomatic, mitral regurgitation who are denied surgery?" *Eur. Heart J.*, vol. 28, no. 11, pp. 1358–1365, 2007.

[5] A. M. Gilliov, M. K. Banbury, and D. M. Cosgrove, "Hemisternotomy approach for aortic and mitral valve surgery," *J. Card. Surg.*, vol. 15, no. 1, pp. 15–20, 2000.

[6] P. Modi, A. Hassan, and W. R. Chitwood Jr., "Minimally invasive mitral valve surgery: A systematic review and meta-analysis," *J. Card. Surg.*, vol. 34, no. 5, pp. 943–952, 2008.

[7] F. Lucà, L. van Garsse, C. M. Rao *et al.*, "Minimally invasive mitral valve surgery: A systematic review," *Minim. Invasive Surg.*, vol. 2013, pp. 1–10, 2013.

[8] J. Seeburger, M. A. Borger, V. Falk *et al.*, "Minimal invasive mitral valve repair for mitral regurgitation: results of 1339 consecutive patients," *Eur. J. Cardiothorac. Surg.*, vol. 34, no. 4, pp. 760–765, 2008.

[9] J. D. Schmitto, S. A. Mokashi, and L. H. Cohn, "Minimally-invasive valve surgery," *J. Am. Coll. Cardiol.*, vol. 56, no. 6, pp. 455–462, 2010.

[10] S. H. Yoon, B. K. Whisenant, S. Bleiziffer *et al.*, "Outcomes of transcatheter mitral valve replacement for degenerated bioprostheses, failed annuloplasty rings, and mitral annular calcification," *Eur Heart J.*, vol. 40, pp. 441–451, 2019.

[11] T. Kansara, A. Kumar, M. Majmundar *et al.*, "Mitral regurgitation following PASCAL mitral valve repair system: A single arm meta-analysis," *Indian Heart J.*, vol. 73, no. 1, pp. 129–131, 2021.

[12] J. Godzik, G. M. Mastorakos, G. Nayar *et al.*, "Surgeon and staff radiation exposure in minimally invasive spinal surgery: Prospective series using a personal dosimeter," *J. Neurosurg.: Spine*, Feb 2020.

[13] D. J. Lanfranco AR, Castellanos AE and M. WC, "Robotic surgery: A current perspective," *Ann. Surg.*, vol. 239, no. 1, pp. 14–21, Jan 2004.

[14] R. M and S. KP, "Robotic-Assisted Percutaneous Coronary Intervention: Rationale, Implementation, Case Selection and Limitations of Current Technology," *J. Clin. Med.*, vol. 7, no. 3, Jan 2018.

[15] MitraClip®. MitraClip® Clip Delivery System. [Accessed: Sept. 1, 2022]. [Online]. Available: https://www.accessdata.fda.gov/cdrh_docs/pdf10/P100009c.pdf.

[16] N. Nayar, S. Jeong, and J. P. Desai, "Towards the development of a robotic transcatheter delivery system for mitral valve implant," in *Proc. IEEE/RSJ Int. Conf. Intell. Robots Syst.*, 2020, pp. 3172–3177.

[17] N. Nayar, S. Jeong, and J. P. Desai, "Design and control of 5-DoF robotically steerable catheter for the delivery of the mitral valve implant," in *Proc. IEEE Int. Conf. Robot. Autom.*, 2021, pp. 12 268–12 274.

[18] Y. Liu and F. Alambeigi, "Effect of External and Internal Loads on Tension Loss of Tendon-Driven Continuum Manipulators," *IEEE Robot. Autom. Lett.*, vol. 6, no. 2, pp. 1606–1613, 2021.

[19] P. Lis, A. Sarma, G. Trimpe *et al.*, "Design and modeling of a compact advancement mechanism for a modified coast guidewire robot," in *Proc. IEEE Int. Conf. Robot. Autom.*, 2022, pp. 1176–1182.

[20] R. Qi, M. Rushton, A. Khajepour *et al.*, "Decoupled modeling and model predictive control of a hybrid cable-driven robot (HCDR)," *Rob. Auton. Syst.*, vol. 118, pp. 1–12, 2019.

[21] R. Xue, B. Ren, Z. Yan *et al.*, "A cable-pulley system modeling based position compensation control for a laparoscope surgical robot," *Mech. Mach. Theory*, vol. 118, pp. 283–299, 2017.

[22] P. E. Dupont, N. Simaan, H. Choset *et al.*, "Continuum robots for medical interventions," *Proc. IEEE*, vol. 110, no. 7, pp. 847–870, 2022.

[23] D. W. H. Tan, P. K. Ng, E. E. M. Noor *et al.*, "Development and usability testing of a finger grip enhancer for the elderly," *Robotics*, vol. 11, no. 1, 2022.

[24] Y.-L. Bai, S.-J. Mei, P. Li *et al.*, "Cyclic stress-strain model for large-rupture strain fiber-reinforced polymer (LRS FRP)-confined concrete," *J. Build. Eng.*, vol. 42, p. 102459, 2021.